NASA CR-2001-210800

# Design and Analysis of a Sun Sensor for Planetary Rover Absolute Heading Detection

*Ashitey Trebi-Ollennu, Terry Huntsberger, Yang Cheng,*
*E. T. Baumgartner, and Brett Kennedy*

*January 2001*

# The NASA STI Program Office ... in Profile

Since its founding, NASA has been dedicated to the advancement of aeronautics and space science. The NASA Scientific and Technical Information (STI) Program Office plays a key part in helping NASA maintain this important role.

The NASA STI Program Office is operated by Langley Research Center, the lead center for NASA's scientific and technical information. The NASA STI Program Office provides access to the NASA STI Database, the largest collection of aeronautical and space science STI in the world. The Program Office is also NASA's institutional mechanism for disseminating the results of its research and development activities. These results are published by NASA in the NASA STI Report Series, which includes the following report types:
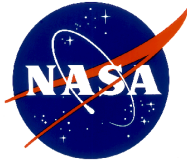
- TECHNICAL PUBLICATION. Reports of completed research or a major significant phase of research that present the results of NASA programs and include extensive data or theoretical analysis. Includes compilations of significant scientific and technical data and information deemed to be of continuing reference value. NASA counterpart of peer-reviewed formal professional papers, but having less stringent limitations on manuscript length and extent of graphic presentations.

- TECHNICAL MEMORANDUM. Scientific and technical findings that are preliminary or of specialized interest, e.g., quick release reports, working papers, and bibliographies that contain minimal annotation. Does not contain extensive analysis.

- CONTRACTOR REPORT. Scientific and technical findings by NASA-sponsored contractors and grantees.

- CONFERENCE PUBLICATION. Collected papers from scientific and technical conferences, symposia, seminars, or other meetings sponsored or co-sponsored by NASA.

- SPECIAL PUBLICATION. Scientific, technical, or historical information from NASA programs, projects, and missions, often concerned with subjects having substantial public interest.

- TECHNICAL TRANSLATION. English-language translations of foreign scientific and technical material pertinent to NASA's mission.

Specialized services that complement the STI Program Office's diverse offerings include creating custom thesauri, building customized databases, organizing and publishing research results ... even providing videos.

For more information about the NASA STI Program Office, see the following:

- Access the NASA STI Program Home Page at ***http://www.sti.nasa.gov***

- E-mail your question via the Internet to help@sti.nasa.gov

- Fax your question to the NASA STI Help Desk at (301) 621-0134

- Telephone the NASA STI Help Desk at (301) 621-0390

- Write to:
  NASA STI Help Desk
  NASA Center for AeroSpace Information
  7121 Standard Drive
  Hanover, MD 21076-1320

NASA CR-2001-210800

# Design and Analysis of a Sun Sensor for Planetary Rover Absolute Heading Detection

*Ashitey Trebi-Ollennu, Terry Huntsberger, Yang Cheng,*
*E. T. Baumgartner, and Brett Kennedy*

*January 2001*

# Abstract

This paper describes a new Sun sensor for absolute heading detection developed for the Field Integrated, Design and Operations (FIDO) rover. The FIDO rover is an advanced technology rover that is a terrestrial prototype of the rovers NASA/Jet Propulsion Laboratory (JPL) plans to send to Mars in 2003. The need for a Sun-sensor on planetary rovers lies in the fact that current means of estimating the heading of planetary rovers involves integration of noisy rotational-speed measurements. This noise causes error to accumulate and grow rapidly. Moreover, the heading error affects the estimate of the x, y position of the rover. More importantly, incremental odometry heading estimation is only reliable over relatively short distances. There is an urgent need to develop a new heading-detection sensor for long traverses (for example, 100 m per Sol [Martian Day]), as outlined for the 2003 Mars mission. Results of a recent FIDO field trial at Black Rock Summit in Central Nevada and several Operations Readiness Test (ORTs) at the JPL MarsYard using the Sun-sensor have demonstrated three- to four-fold improvement in the heading estimation of the rover compared to incremental odometry. These test results helped shape the mission specifications outlined by NASA for the 2003 mission to Mars.

# Acknowledgment

Available from:

NASA Center for AeroSpace Information
7121 Standard Drive
Hanover, MD 21076-1320
301-621-0390

National Technical Information Service
5285 Port Royal Road
Springfield, VA 22161
703-605-6000

# Table of Contents

# Tables

# Figures

# 1  Introduction

The successful use of celestial navigation sensors (e.g., Sun sensors and star trackers) by spacecraft and marine vehicles have attracted great interest in their use by planetary robotists because there are currently no immediate plans by NASA to install Global Positioning Systems (GPS) for other planets.  Magnetic heading detection devices are not viable because most of the planets in our solar system have negligible magnetic fields.  Absolute heading detection for planetary rovers remains the most significant of the navigation parameters in terms of its influence on accumulated dead-reckoning errors.  For example, in an odometry-based positioning rover, any small orientation error will cause a constant growing lateral position error.  Therefore, sensors that can provide a measure of absolute heading are of extreme importance in developing long-range navigation algorithms for future autonomous planetary rovers.

Of all the celestial bodies, the Sun is the most attractive for navigation.  In the past twenty years, a Sun sensor has been used on every satellite launched for both attitude determination and attitude control.  Two key factors (Wertz 1995) make the Sun the most attractive celestial body for navigation.  Firstly, the Sun is sufficiently bright; it is, therefore, easy to detect without the need to discriminate among other celestial sources.  Secondly, the Sun's angular radius is nearly orbit independent and sufficiently small (0.267 degrees at 1 AU) that it suffices to model it as a point source.

In 1998, Doraiswami (Doraiswami 1998) developed a Sun sensor for planetary rovers consisting of a lateral-effects sensor located at the focal plane of a system of lenses that capture the incoming sunlight.  The lateral-effects sensor functions as a two-dimensional photo diode that locates the position of the sunlight focused on the detector surface.  The Sun sensor outputs four signals corresponding to the distance of the focus light from each of the four corners of the sensor plane.  Using a robust Kalman filter estimation scheme, the x- and y-position coordinates of the sunlight in the sensor frame is computed.  The redundancy in the measurement is exploited to detect and isolate erroneous sensor measurement.  However, the developed Sun sensor was never used on a real rover and is computationally expensive for real-time implementation.

Volpe (Volpe 1999) reports the use of a Sun sensor in long-range mission scenario field trials on ROCKY 7, a Mars rover at JPL.  The Sun sensor is very similar to the Sun sensor developed by Doraiswami (Doraiswami 1998) and was developed by Lockheed Martin Astronautics, Denver, at a cost of more than $30,000.

The Sun sensor outputs analog signals proportional to the centroid of the sunlight intensity image. Although the Sun sensor update rate is relatively fast, with very little computation, it requires a fairly complex calibration process. Any slight miscalibration leads to significant errors in the output.

The goal of the Field Integrated, Design and Operations (FIDO) team was to develop a Sun sensor that fills the current cost/performance gap, uses the power of sub-pixel interpolation, makes use of current hardware on the rover, and demands very little computational overhead. In addition, a great deal of emphasis was placed on robustness to calibration errors and the flexibility to make a transition to a flight rover with very little modification. The resulting Sun sensor, which is shown in Figure 1, consists of a charge-coupled device (CCD) monochrome camera, two neutral-density filters, a wide-angle lens (FOV $120 \times 84$ degrees), and housing (shown in Figure 2 ). Figure 1 depicts the Sun sensor mounted on FIDO. The neutral-density filters are attached to the camera lens so that the Sun can be observed directly. The neutral-density filters reduce incident light to capture only the Sun's disk. The Sun sensor camera is modeled as a fish eye camera/lens system with 21 parameters; the parameters are computed in the calibration procedure (Y. Xiong 1997). The Sun sensor captures images of the Sun using an onboard frame grabber mounted on the rover PC/104 stack.
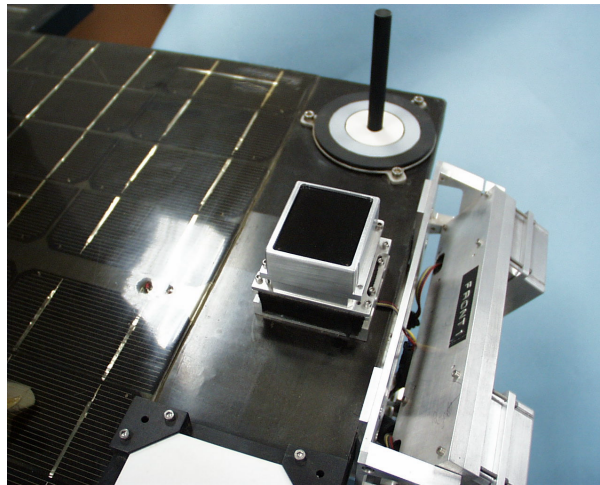


**Figure 1. Sun Sensor Mounted on the FIDO Rover**
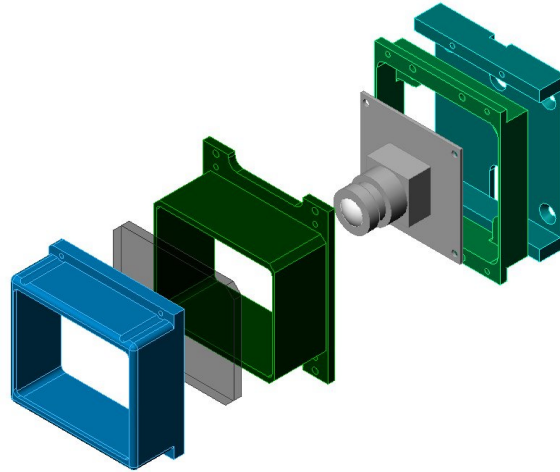
**Figure 2. Exploded Component Suite of the Sun Sensor**

The sections of this paper that follow are organized as follows:

- Section 2 presents a brief description of FIDO rover.

- Section 3 presents a detailed description of the concepts and formulation of the Sun sensor algorithm.

- Section 4 presents experimental and sensitivity-analysis results of the Sun sensor.

- Section 5 presents conclusions.

## 2  FIDO Rover

The FIDO rover is an advanced technology rover that is a terrestrial prototype of the rover that NASA/JPL plans to send to Mars in 2003. FIDO's mobility sub-system consists of a six-wheel rocker-bogie suspension system (Randel Lindemann 1999) and is capable of traversing over obstacles up to 30 cm in height. FIDO is equipped with an analog of the science payload that the flight rover will carry.

FIDO has a 4-degrees-of-freedom (DOF) mast that extends to 1.94 m when deployed (as shown in Figure 3). When the vehicle is moving, the mast is stowed on the rover deck. The mast-head houses a stereo PanCam (panorama camera), a stereo NavCam (navigation camera), and an Infrared Point Spectrometer (IPS). The PanCam has a three-band color imaging system capable of surveying the terrain in stereo with high-resolution spatial resolution for scientific purposes. The NavCam is a low-spatial-resolution, monochrome, wide-field-of-view stereo imaging system used for traverse planning. The IPS is bore sighted with NavCam and PanCam (Baumgartner 2000) and is used to acquire spectral radiance information in either a point or raster mode. In addition to the mast, FIDO has a 4-DOF Instrument Arm, a Mini-Corer, and BellyCam (a stereo camera) mounted on the underside or "belly" of the front of the rover. A color microscopic imager is mounted on the end-effector of the Instrument Arm. The Mini-Corer can be used to acquire sample cores from rocks of 0.5-cm diameter and up to 1.7 cm long.

The activities of the Instrument Arm and Mini-Corer are monitored and coordinated via the BellyCam. In addition to the NavCam, FIDO has two other sets of stereo cameras, called the Front HazCam and the Rear HazCam. The autonomous hazard avoidance algorithm for obstacle detection during rover traverse uses the HazCams.



**Figure 3. FIDO Rovers with the Mast and Instrument Arm Deployed at Black Rock summit in Nevada, USA**

The rover-computing platform is a PC/104 266Mhz, Pentium-class CPU with a VxWorks 5.3 real-time operating system. FIDO uses three-layer software architecture: the lowest layer is the Device Driver Layer (DDL), the middle layer is the Device Layer (DL), and the top layer is called Application Layer (APL). The DDL handles all hardware dependencies (e.g., DIO, Counters, A/D drivers). The DDL provides the means for abstracting the higher-level software in the APL from the hardware dependencies. The DDL is responsible for all motion-control functions, vision processing, instrument interfaces, forward and inverse kinematics for the Mast and Instrument Arm, etc. (E. T. Baumgartner 2000). The APL contains all rover sequences, instrument sequences, Sun sensor algorithm, and hazard-detection and path-planning software. The software on FIDO is written in ANSI-C.

FIDO has been used to simulate operational concepts for future Mars surface exploration missions. Recent blind field tests (May 2000) in Black Rock Summit in Nevada helped shape the rover mission specifications outlined by NASA for 2003 mission to Mars.

During field trials (R. E. Arvidson 2000), operations are directed from JPL by actual Mars mission flight science team members and distributed collaborative users all over the world via the Internet. The Web Interface for Telescience (WITS) and the Multi-Mission Encrypted Communication System (MECS) (Paul G. Backes 2000) are used for sequence planning and generation and command and data product recovery.

# 3  Sun Sensor

This section outlines the detailed concepts and formulation of the Sun sensor algorithm.

## 3.1  Camera Model

To correctly predict 3-D rays of objects from their respective camera 2-D images, a geometric calibration of the camera is required.  Geometric calibration of a camera entails correctly modeling the optical path of the camera.  A typical approach to geometric calibration of a camera is to take an image of a precisely known target and use the geometric properties of the target to determine the lens and camera parameters.  Figure 4 depicts a camera calibration target used at JPL's robotics laboratory.  The camera target has three one-square-meter components that are made from aluminum and anodized to have a dull, matte black color.  As shown in Figure 4, each face of the calibration targets has a $10 \times 10$ grid of 2-inch diameter white circles (or dots) stamped on it.  The three faces are assembled to form the "inside corner" of a cube.  The camera calibration process relies on the accurate detection of the centroid of the white dots found on each face of the calibration target.
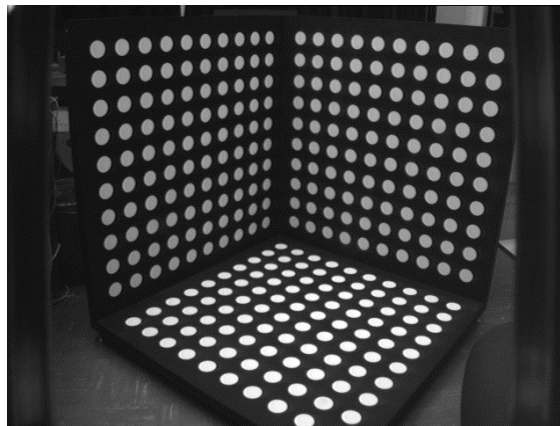


**Figure 4. Picture of Calibration Target**

The basic camera model used at JPL's robotics laboratory is comprised of six 3-vector parameters — **c**, **a**, **h**, **v**, **o**, and **r** (**cahvor**) — expressed in object-coordinate frame (Gennery ).  Parameter **c** defines the position of the perspective center of the camera lens (focal center).  Parameter **a** is a unit vector pointing outwards from the camera and parallel to a perpendicular from the exist pupil pointing to the image sensor plane.  Parameters **h** and **v** are vectors in the sensor plane and are perpendicular to the x and y image axes, respectively (**h** and **v** are not necessary orthogonal).  Parameter **o** is a unit vector used to represent the optical axis.  The radial distortion polynomial of the camera lens system is defined relative to **o**.

However, the **cahvor** lens camera model cannot adequately model the Sun sensor camera because a wide-field-of-view (FOV) (120 degrees) lens is being used.  Therefore, an extension of the **cahvor** camera model, known locally as **cahvore,** was used.  The major difference between **cahvor** and **cahvore** is that the **cahvore** assumes the entering ray is projected at $r = f\rho$ instead of $r = f \tan \rho$, where $\rho$ is the angle between the entering ray and the optical axis. $f$ is the focal length of the lens and $r$ is the offset from the center of the image plane.  The **cahvore** performance is much better when the FOV is large ($\geq 100^{o}$).

The camera calibration algorithm uses nonlinear least squares adjustments to operate on a calibration target image.  The camera model parameters are adjusted to minimize the sum of the squares of the residuals in the image plane.  During calibration of the Sun sensor camera, the camera was rigidly mounted in front of the calibration target shown in Figure 4.  The camera was aimed directly at the point where all three faces of the target meet.  The camera position was iteratively adjusted until the two vertical faces of the target covered most of the image.  The image was run through the camera-calibration algorithm described above to generate a 21-parameter camera model.  The resulting camera coordinate frame is shown in Figure 8.

## 3.2   Feature Extraction

The centroid of the Sun in the image is the main feature needed for determination of the rover heading.  The neutral density filters in the Sun sensor assembly filter out the majority of the low-level light.  Centroid extraction follows a three-step process: thresholding, artifact removal, and center of mass/circularity determination.  The thresholding operation is based on a fixed threshold that has been experimentally determined using a standard Sun sensor assembly.  Artifact removal is performed using mathematical morphology operations on the thresholded image.  Finally, the first and second order shape moments are extracted from the thresholded image to determine the centroid (center of mass) and the circularity.

The neutral density filters reduce incident light to capture only the Sun disk.  However, the filters may also capture reflections of the Sun onto clouds and secondary reflections from the surface of the lens assembly.  Both of these types of artifacts can potentially influence the accuracy of the centroid determination.  An example of a raw Sun sensor image is shown in Figure 5.  This image has all three types of artifacts and also includes blooming of the CCD sensor from saturation.   We have defined a confidence measure based on the relative percentage of blooming and cloud cover or haze in the image.  The confidence measure is used for decision making during the Extended Kalman Filter update of the rover heading.  This confidence measure is given by:

$$confidence\_measure = 1.0 - \frac{confidence\_count}{Size - count} \qquad \textbf{Equation 1}$$

where *Size* is the total image size in pixels, *count* is the total number of pixels above the threshold for Sun pixel candidates (gray scale value of 220), and *confidence_count* is the total number of pixels that have a threshold greater than an experimentally determined background level (gray scale value of 70) and less than the Sun pixel threshold. This measure will be 1.0 if all pixels in the image are Sun-pixel candidates. It does not include the spatial effect of multiple regions that are above the Sun-pixel threshold. The confidence measure for the Sun image in Figure 5 is 0.896.



**Figure 5. Original Sun Sensor Image**
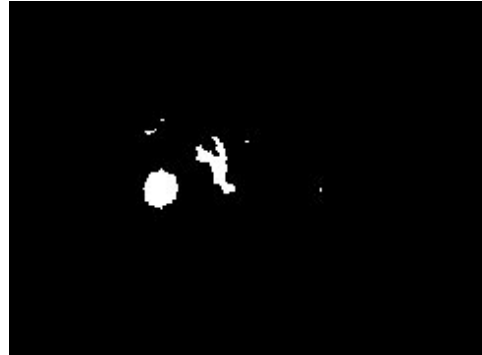


**Figure 6. Image After Threshold Operation**
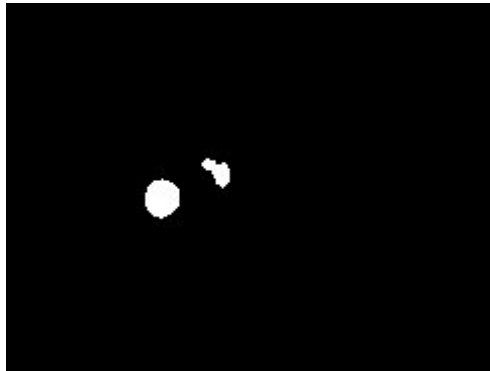


**Figure 7. Image After Application of Open Operation**

The output of the thresholding operation on the image in Figure 5 is shown in Figure 6, where all pixels below the threshold have been set to zero. The blooming has been eliminated. In addition, most of the clouds — with the exception of those closest to the Sun — have also been suppressed. Small secondary reflections appear as isolated point-like structures throughout the image. The mathematical morphology *open* operation is used to further suppress the smaller cloud and secondary reflection artifacts.

The *open* operator $O_{AB}(a)$ is defined as (R.M. Haralick 1987):

$$O_{AB}(a) = D_{AB}(a)[E_{AB}(a)] \qquad \text{\textbf{Equation 2}}$$

where $E_{AB}$ and $D_{AB}$ are, respectively, the erosion and dilation operations on image *A* with a structuring element *B* centered at position *a*. Erosion is the minimum value of the pixels within a specified neighborhood. Dilation is the maximum value within the same neighborhood. This operation has the effect of removing any objects that are less than the neighborhood size and is usually used for noise removal. We use the operator to remove objects that would not be good Sun candidates due to size. The output of the application of the operator to the thresholded image of Figure 6 is shown in Figure 7, where the smaller artifacts caused by clouds and secondary reflections have been eliminated. All that remains are two regions: the Sun and the closest cloud-patch, which has been reduced to a compact shape.

The primary difference between the Sun region and the cloud artifact is the circularity of the Sun. The first-order shape moments are defined as (Levine 1985):

$$Centroid_x = \frac{\sum_A x}{Area}, \; Centroid_y = \frac{\sum_A y}{Area}, \qquad \text{\textbf{Equation 3}}$$

where *Area* is the area of the region with non-zero pixels and *x* and *y* are the coordinates within this region. In the event that there is more than one region (as seen in Figure 7), a region-growing process must be run first, followed by the first-order shape-moment extraction. This will result in more than one centroid being found; some other process must be used to determine which region corresponds to the Sun. We use the second-order shape moments $\mu_{11}, \mu_{02}$, and $\mu_{20}$ to evaluate the circularity and standard deviation of each region. These operators are defined as:

$$\mu_{11} = \sum_A \left( (x - Centroid_x)(y - Centroid_y) \right)$$
$$\mu_{02} = \sum_A \left( y - centroid_y \right)^2 \qquad \text{\textbf{Equation 4}}$$
$$\mu_{20} = \sum_A \left( x - centroid_x \right)^2$$

The standard deviation is defined as:

$$\sigma_x = \left[ \frac{\mu_{20}}{Area} \right]^{\frac{1}{2}}, \sigma_y = \left[ \frac{\mu_{02}}{Area} \right]^{\frac{1}{2}} \qquad \text{\textbf{Equation 5}}$$

This measure is used to determine whether there is a significant deviation from circularity in any given direction.

This measure is position independent. A circular region is characterized by $\mu_{11} = 0$. We will use the relative magnitude to determine the circularity of a region. For the two regions in Figure 7, the value of $\mu_{11} = -9710$, $\sigma_x = 11.39$, and $\sigma_y = 12.46$ for the Sun and $\mu_{11} = 37985$, $\sigma_x = 9.43$, and $\sigma_y = 9.20$ for the cloud artifact.
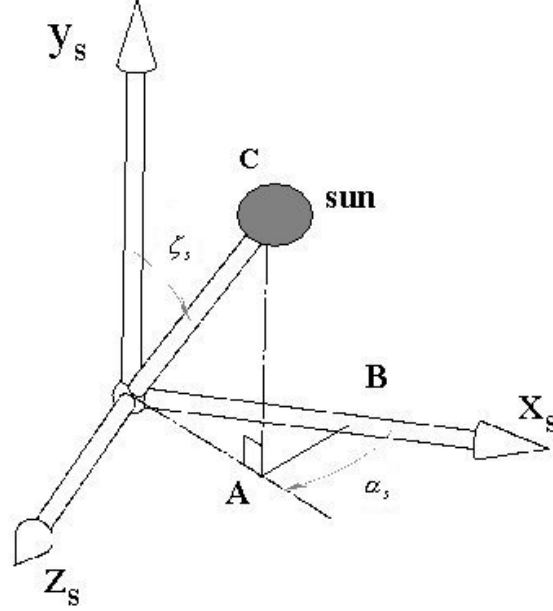


**Figure 8. Sun Sensor Coordinate Frame**

### 3.3 Sun Azimuth and Elevation Computation Using Sun Sensor

Given the 2-D Sun centroid from the threshold Sun image, a 3-D unit ray vector $s = \begin{bmatrix} s_x & s_y & s_z \end{bmatrix}^T$ is computed from the sensor to the Sun using the camera model. Given the Sun's azimuth ($\alpha_s$) and elevation ($\zeta_s$) in the sensor frame as shown Figure 8, the components of the 3-D unit ray vector $s$ can be determined as follows:

$$CA = \cos\zeta_s, \quad OA = \sin\zeta_s, \quad BA = \sin\alpha_s \sin\zeta_s, \text{ and } OB = \cos\alpha_s \sin\zeta_s \qquad \textbf{Equation 6}$$

From equation (6), $s = \begin{bmatrix} s_x & s_y & s_z \end{bmatrix}^T$ is defined as:

$$\begin{bmatrix} s_x \\ s_y \\ s_z \end{bmatrix} = \begin{bmatrix} \cos\alpha_s \sin\zeta_s \\ \cos\zeta_s \\ \sin\alpha_s \sin\zeta_s \end{bmatrix} \qquad \textbf{Equation 7}$$

The 3-D unit ray vector $s$ is transformed to the rover frame as $s_R = \begin{bmatrix} s_{Rx} & s_{Ry} & s_{Rz} \end{bmatrix}^T$, where the components of $s_R$ are defined as follows:

$$\begin{bmatrix} s_{Rx} \\ s_{Ry} \\ s_{Rz} \end{bmatrix} = \begin{bmatrix} 0 & 0 & 1 \\ -1 & 0 & 0 \\ 0 & -1 & 0 \end{bmatrix} \begin{bmatrix} s_x \\ s_y \\ s_z \end{bmatrix} \qquad \textbf{Equation 8}$$

The transformation matrix from the sensor frame to rover frame can be derived from Figure 9 and Figure 10 by inspection. From equation (7) and equation (8), the Sun's azimuth and elevation can be computed in the sensor and rover frame respectively. However, we are interested in computing the heading of the rover in the site fixed gravity-down reference frame. The 3-D unit ray $s_R$ is transformed to the site-fixed gravity-down reference frame. The site-fixed gravity-down reference frame is depicted in Figure 9 and Figure 10. The $x_{site}$-axis is aligned to True North, the $y_{site}$-axis is aligned to East, and the $z_{site}$-axis points downward parallel to gravity. In general, the rover is usually True North aligned before the start of a mission. Let us assume that the rover coordinate frame is aligned with the site-fixed gravity-down reference coordinate frame (i.e., the rover is level and pointing to True North). The orientation of the rover changes as it drives over undulating natural terrain. On FIDO, the rover's orientation is obtained from an onboard inertial navigation sensor. The inertial navigation sensor has three rate gyros and three accelerometers for measuring rover angular rates and accelerations, respectively. Currently, only the accelerometers are used to estimate the rover's pitch and roll.
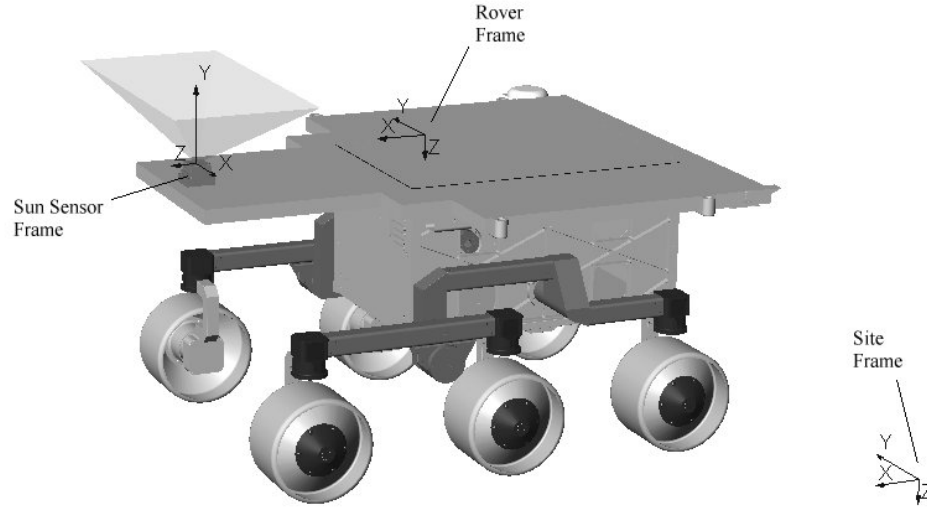


**Figure 9. Rover, Sun Sensor, and Site Frames with Illustrative Pyramid for Sun Sensor Field of View**
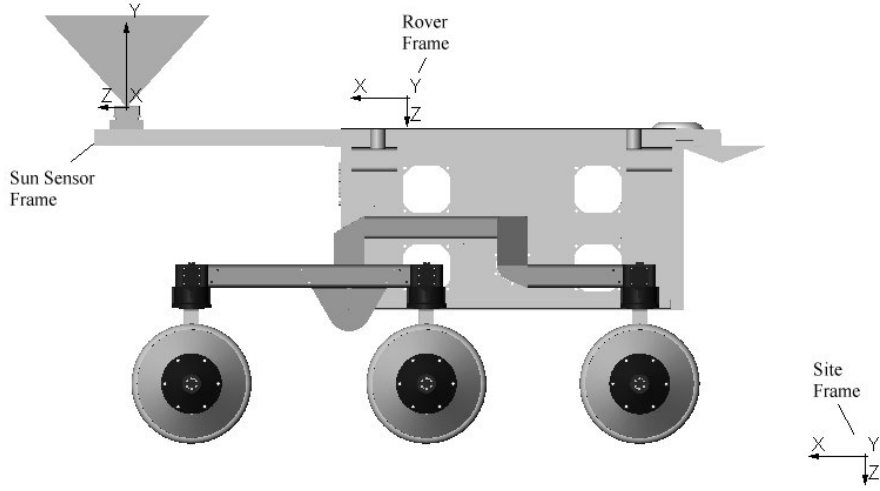
**Figure 10. Profile of Rover, Sun Sensor, and Site Frames**

To derive the rotational matrix that will transform the rover from any given orientation to the level coordinate frame, we must assume that the rover is stationary and the rover coordinate frame is coincident with the level frame (i.e., a site-fixed reference frame). If the rover is pitched $\theta$ about the rover $y_R$-axis and rolled $\phi$ about the rover $x_R$-axis, the rover's position vector in the rover frame can be expressed as follows (D. H. Titterton 1997):

$$\begin{bmatrix} x_R \\ y_R \\ z_R \end{bmatrix} = \begin{bmatrix} 1 & 0 & 0 \\ 0 & \cos\phi & \sin\phi \\ 0 & -\sin\phi & \cos\phi \end{bmatrix} \begin{bmatrix} \cos\theta & 0 & -\sin\theta \\ 0 & 1 & 0 \\ \sin\theta & 0 & \cos\theta \end{bmatrix} \begin{bmatrix} x_{site} \\ y_{site} \\ z_{site} \end{bmatrix}$$ **Equation 9**

The order of the rotation is of fundamental importance because these operators are not commutative. From equation (9), the rotation matrix for transforming points in the site-fixed, reference-coordinate frame to the rover frame is determined as:

$$T = \begin{bmatrix} \cos\theta & 0 & -\sin\theta \\ \sin\phi\sin\theta & \cos\phi & \sin\phi\cos\theta \\ \cos\phi\sin\theta & -\sin\phi & \cos\phi\cos\theta \end{bmatrix}$$ **Equation 10**

During initial alignment, the rover is assumed stationary. The velocities and accelerations of the rover can be considered to be zero (except for gravity). The rover's acceleration at stand still is $\lambda = \begin{vmatrix} 0 & 0 & g \end{vmatrix}$, where g is gravity. The rover's stationary acceleration in the rover frame can be expressed as follows using equation (9), (Aleksandr Brandt 1998) and (*Nebot* 1997):

$$\begin{bmatrix} a_{Rx} \\ a_{Ry} \\ a_{Rz} \end{bmatrix} = \begin{bmatrix} -\sin\theta \\ \sin\phi\cos\theta \\ \cos\phi\cos\theta \end{bmatrix} g$$ **Equation 11**

From equation (11), the component of the rotational matrix equation (10) can be determined in terms of the rover's acceleration in rover frame as follows:

$$\sin\theta = -a_{Rx} \qquad \text{Equation 12}$$

From trigonometry identities, $\sin^2\theta + \cos^2\theta = 1$ and equation (12),

$$\cos\theta = \sqrt{1 - (a_{Rx})^2} \equiv v \qquad \text{Equation 13}$$

From equations (11, 12, and 13),

$$\sin\phi = \frac{a_{Ry}}{v} \text{ and } \cos\phi = \frac{a_{Rz}}{v} \qquad \text{Equation 14}$$

In the case of rotating the 3-D unit ray $s_R$ to the site-fixed gravity-down reference frame, the inverse of the rotational matrix in equation (10) is required. However, the rotational matrix of equation (10) is a special orthogonal matrix where $T^{-1} = T^T$. The rotational matrix for rotating from the rover frame to the site-fixed reference frame is given by:

$$G = T^T = \begin{bmatrix} v & \dfrac{-a_{Ry}a_{Rx}}{v} & \dfrac{-a_{Rz}a_{Rx}}{v} \\ 0 & \dfrac{a_{Rz}}{v} & \dfrac{-a_{Ry}}{v} \\ a_{Rx} & a_{Ry} & a_{Rz} \end{bmatrix} \qquad \text{Equation 15}$$

The 3-D unit ray $s_{site} = \begin{bmatrix} s_{sx} & s_{sy} & s_{sz} \end{bmatrix}^T$ is obtained as follows:

$$s_{site} = Gs_R \qquad \text{Equation 16}$$

The azimuth $\alpha_{site}$ and elevation $\zeta_{site}$ of the Sun in the site-fixed gravity-down reference frame can be computed as follows:

$$\alpha_{site} = a\tan2(s_{sx}, s_{sy}) \text{ and } \zeta_{site} = \sin^{-1}(s_{sz}) \qquad \text{Equation 17}$$

### 3.3.1 Sun Azimuth and Elevation Computation Using Ephemeris Data

For a given Universal Time (UT), the astronomical position of the Sun is fixed and can be obtained from The Astronomical Almanac. A real-time algorithm was developed from a shareware program obtained from Astronomy and Numerical Software Source Codes Web site (Moshier 1987). The program was significantly modified to simplify it and make it computational efficient for real-time implementation. The algorithm uses solar ephemeris data and solves Kepler's equation and the equation of time to determine the position of the Sun (azimuth and elevation) for a given geodetic longitude, latitude, and UT. UT is obtained from the rover computer clock and corrected to the nearest second. From UT, Julian Day is computed and transformed to Ephemeris Time. Although the algorithm is fairly robust, it is not suitable for a flight rover because it does not meet flight software validation requirements. However, it has proved very useful for research and development. All results presented in this paper are based on it.

We are currently working with The Navigation and Ancillary Information Facility (NAIF) at JPL to adapt or develop a rover Sun sensor toolkit from JPL's **S**pacecraft **P**lanet **I**nstrument **C**-matrix **E**vents (SPICE) information system. SPICE assists scientists and engineers involved with mission evaluation, mission operations, observation planning, and science data analysis. The new algorithm will be developed using Chebyshev polynomials to approximate a set of ephemeris data from a known start date to a known end date. The advantage of Chebyshev polynomials lies in the fact that they oscillate about zero with peak deviations that are bounded and equal. Approximating a data set in terms of Chebyshev polynomials allows a trade off of small errors near zero for fewer errors near the extremes of the data range. The coefficients of the Chebyshev polynomials would be computed a priori. This would significantly speed up the computation. For a given Ephemeris Time, the Sun's position from a specified surface point on a planet (e.g., Earth) can be determined by solving the Chebyshev polynomials and correcting for light time and stellar aberration. The Sun state is defined relative to the fixed surface point.

### 3.3.2   Rover Heading Computation

Using the Sun position (azimuth and elevation) from the Sun-sensor and solar ephemeris data, the rover's absolute heading with respect to True North is computed. For a given longitude, latitude, altitude, and UT, the astronomical and Sun sensor position of the Sun are determined as described above. If the astronomical position of the Sun is determined by azimuth $\alpha_{astron}$ and elevation $\zeta_{astron}$ and the Sun sensor position of the Sun is determined by azimuth $\alpha_{site}$ and elevation $\zeta_{site}$ (both are measured in degrees with respect to True North), the rover's heading with respect to True North (in degrees) is computed as follows:

$$If\left(\alpha_{astron} > \alpha_{site}\right)$$
$$Rover\_Heading = \alpha_{astron} - \alpha_{site} + \delta_{bias}$$
$$else$$
$$Rover\_Heading = \alpha_{site} - \alpha_{astron} + \delta_{bias}$$

**Equation 18**

where $\delta_{bias}$ is a systematic bias term that can be determined from experimentation. The bias term can be attributed to several factors, including: elevation of the Sun, 2-D centroid location in the sensor image plane, mechanical misalignment of the sensor with the rover's x-axis, and the CCD camera misalignment in the Sun sensor housing. The outlined Sun sensor algorithm was implemented in ANSI-C in the application layer of the FIDO software architecture.

## 4   Experimental Results and Analysis

An experiment was conducted with FIDO placed on a flat surface and incrementally turned in place at increments of about 20 degrees. Figure 11 depicts FIDO rover headings recorded by a magnetic compass and Sun sensor from the experiment. The Sun sensor confidence for each reading is also indicated on the plot.

In addition, Figure 11 depicts the error between the compass and Sun sensor readings, which is within ± 3 degrees. The accuracy of the magnetic compass used is ±2 degrees. Similar results were obtained with the Sun sensor in the field trials (May 2000) and the operation readiness test. The errors can be attributed to several factors, including mechanical alignment errors of the Sun sensor, rover attitude errors, and atmospheric conditions (cloud cover). The sections that follow describe the sensitivity analysis conducted to determine the dominant factors or parameter uncertainties that adversely affect the output of the Sun sensor.
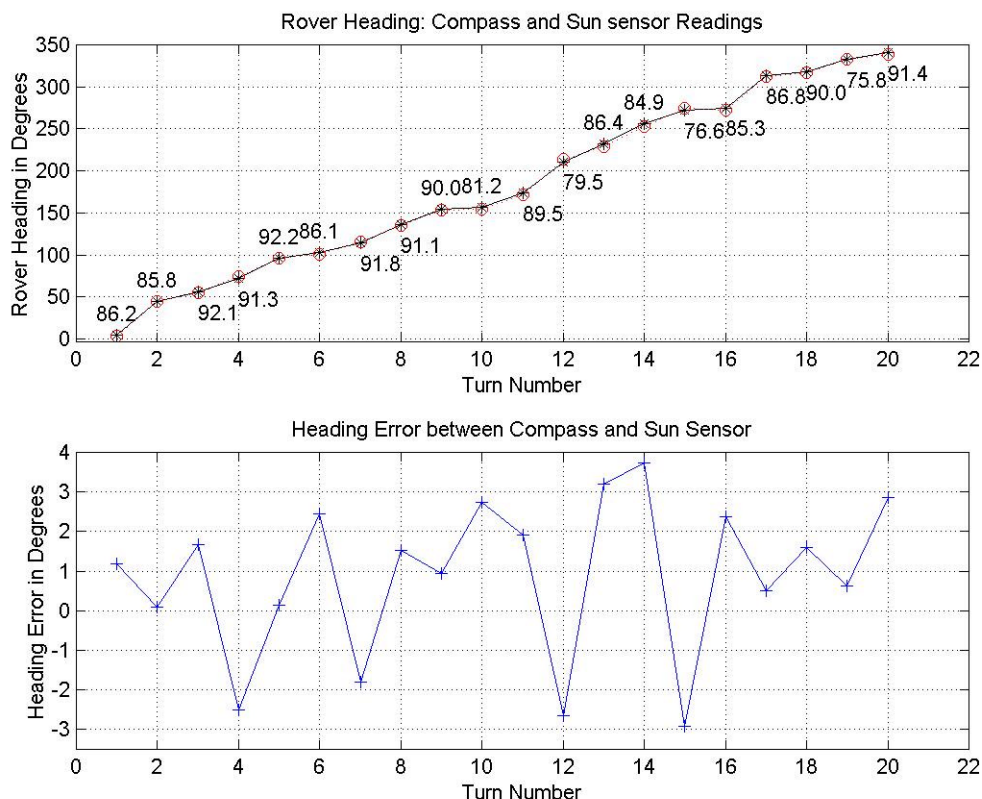


**Figure 11. A Plot of Rover Heading from Compass (*) and Sun Sensor (o)**

## 4.1   Sun Sensor Sensitivity Analysis

In this section, we present an analysis of the impact of parametric uncertainty on the performance of the Sun sensor. In general, parametric models obtained using physical system modeling (e.g., a camera model), parameter estimation (e.g., the Sun's centroid estimation in image plane), or a combination of both will be subject to uncertainty in some, if not all of the parameters. In this analysis, we will characterize (i.e., quantify) and assess the dominate parametric uncertainties and their effect on the performance of the Sun sensor. Methods for analyzing uncertainties overall assume unstructured uncertainty, which means only information concerning the upper bound on the magnitude of the perturbation measured is employed.

In practice, uncertainty is generally structured because it is associated with specific model parameters or may be formulated in terms of norm-bounded perturbations of dominate and distinct elements within the system. Perturbations typically used to describe unstructured uncertainties are additive and multiplicative models. The multiplicative perturbation model is more useful than the additive perturbation model because it represents the uncertainty in a relative manner, rather than an absolute manner. Consider, for example, a multiplicative perturbation $\Delta_m$ bounded as follows, $\|\Delta_m\| \leq 0.3$. This implies the size of the perturbation does not exceed 30% of the nominal model. In the analysis to be presented in this section, only multiplicative perturbation models will be used.

In general, some ingenuity is usually required in selecting the dominant and distinct elements, or states, of a system to be used to formulate parameter uncertainty. This approach relies heavily upon the designer's knowledge and experience of what is technically feasible and practical. In the case of the Sun sensor, they are several candidates: the camera model, an estimate of 2-D Sun image centroid, Sun elevation, and the attitude (roll and pitch) of the rover. Uncertainties in the camera model parameters are beyond the scope of this paper. The interested reader is referred to (Y. Xiong 1997). Sensitivity analysis of the Sun sensor will focus on perturbation models for Sun centroid, Sun elevation, and rover attitude.

### 4.1.1 Impact of Sun Centroid Uncertainty on Sun Sensor Output

Section 3.2 presented the procedure for the estimation of a Sun image 2-D centroid and corresponding confidence. The complement of the confidence measure is, in effect, the degree of uncertainty in the 2-D centroid estimate.

#### *4.1.1.1 2-D Centroid Position Dependent Error*

To determine the error introduced by uncertainties in the estimated position of the 2-D centroid, the geometry of the imaging system comes into play. This geometry is shown in Figure 12, where *f* is the focal length of the lens and *x* is the offset from the center of the image plane. The error for determination of the angle $\varphi$ is given by:

$$\delta\varphi = \frac{f}{\left(f^2 + x^2\right)}$$

**Equation 19**

The relative error/pixel decreases quadratically with distance from center of the image plane. The focal length for the lens is 2.5 mm; the width of the image plane is 8.4 mm. This geometry gives an error of 0.3 degrees/pixel in the center of the image, as shown in Figure 13, Figure 14, and Figure 15. These figures give alternate views of the angular error based on lens characteristics. The contour plot in Figure 14 illustrates that the error has decreased by 16% to 0.25 at 20 pixels away from the center of the image.
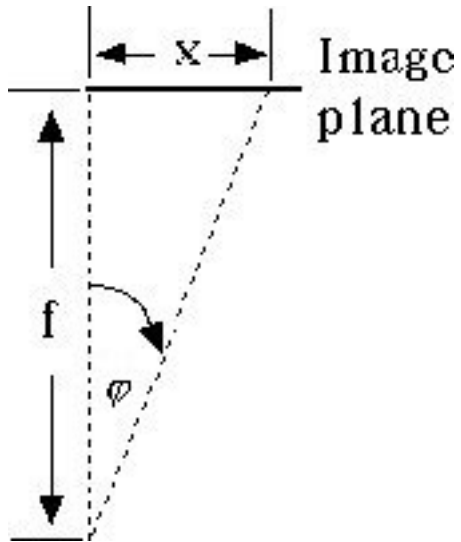
**Figure 12. Geometry for Calculation of Position-Dependent Angular Error**
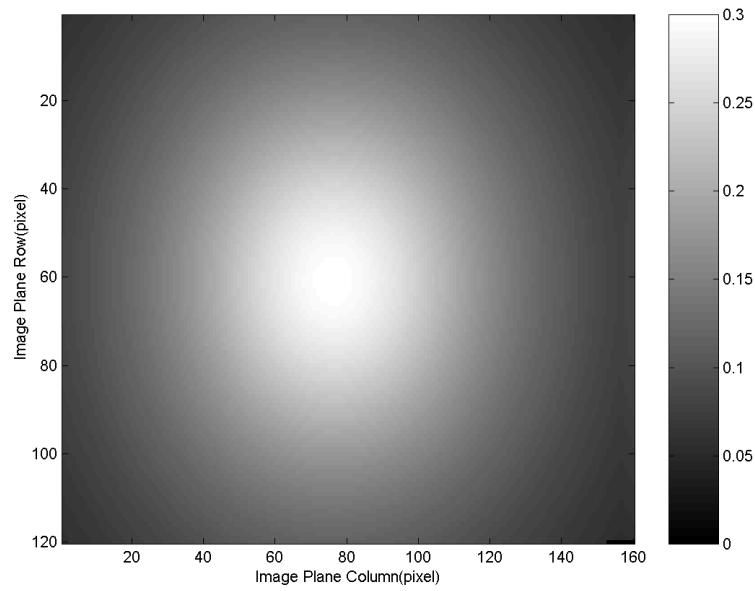


**Figure 13. 2D-Centroid Position Relative Error/pixel Plot in Image Plane (120 × 160 Pixels)**
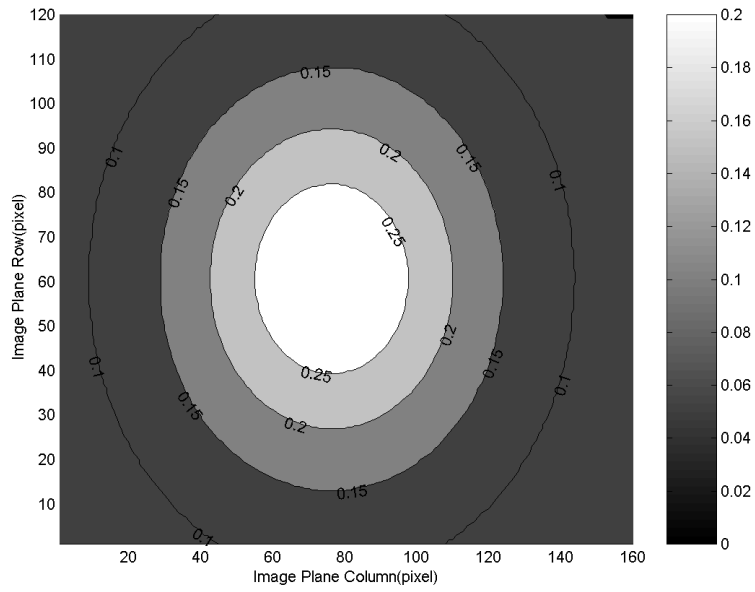
**Figure 14. Contour Plot of 2D-Centroid Position Relative Error/pixel Image Plane (120 × 160 Pixels)**
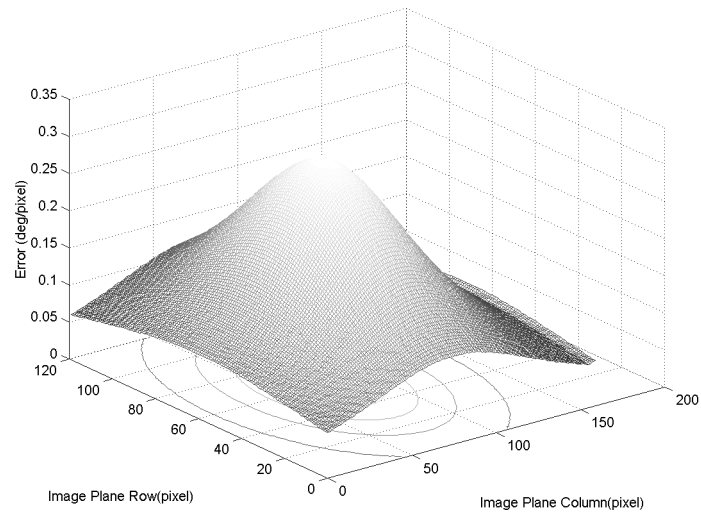


**Figure 15. 3D plot of 2D-Centroid position relative error/pixel plot in image plane (120 × 160 pixels)**

Another error source is the heading error in the estimation of centroid of the Sun. This heading uncertainty $\xi$ can be calculated as $\xi = \dfrac{s}{r}$, where s is the uncertainty in the centroid location and r is the distance from the center of the image. This measure is undefined at the exact center of the image; however, at 1 pixel away the measure is equal to 57.3° for a centroid uncertainty of 1 pixel. This is by far the main source of error in heading determination. The above analysis helped determined a cut-off region for centroid location in the image plane. A centroid located within a 20-pixel radius from the center of the image is discarded. In the cut-off region, an uncertainty of 1 pixel in the centroid will result in at least 2 degrees heading error; this is not acceptable.

### 4.1.2 Impact of Rover Attitude Uncertainty on Sun Sensor Output

As stated earlier, the FIDO rover is equipped with onboard an inertial navigation sensor (INS) to provide attitude information (roll and pitch) and attitude-rate information (roll rate, pitch rate, and heading rate). Uncertainty in the rover attitude may be a result of sensor imperfection, computational errors, and alignment errors. In addition, during rover traverse, the onboard INS may be subjected to nonlinear vibration; such motion arises as a result of rover wheels terrain interaction.

Let $\Delta_a$ be a block-diagonal matrix structure containing norm-bounded perturbations of the rover attitude roll and pitch, as follows:

$$\Delta_a = \begin{bmatrix} \delta_\phi & 0 \\ 0 & \delta_\theta \end{bmatrix} \text{ and } \|\delta_\phi\| \le \vartheta_\phi \text{ and } \|\delta_\theta\| \le \vartheta_\theta \qquad \textbf{Equation 20}$$

where $\delta_\phi$ and $\delta_\theta$ represents the multiplicative perturbations and $\vartheta_\phi$ and $\vartheta_\theta$ represent norm-bounds in the roll and pitch attitude of the rover, respectively. If the attitude of the rover is $A_r = [\phi, \theta]^T$, a multiplicative perturbation model for the rover attitude can be expressed as follows:

$$\delta_\phi \le \vartheta_\phi \phi \text{ and } \delta_\theta \le \vartheta_\theta \theta \qquad \textbf{Equation 21}$$

Equation (21) represents a relative measure of the uncertainty in terms of the nominal value. Using equation (21) the rover attitude can now be expressed as follows,

$$A_r \le \begin{bmatrix} \phi(1 + \vartheta_\phi) \\ \theta(1 + \vartheta_\theta) \end{bmatrix} \qquad \textbf{Equation 22}$$

Using equation (22), a complete sensitivity analysis of rover attitude uncertainties and its impact on the Sun sensor output can be investigated.

An experiment was setup on a cloudless day at JPL in Pasadena, California. The rover was positioned such that the Sun was within the field of view of the Sun sensor. The rover's attitude was as follows: roll $= -0.906476$ degrees and pitch $= -15.446365$ degrees. Using the Sun sensor, an image of the Sun was captured at 13 hours, 57 minutes, 27 seconds on 31 October 2000. The 2-D centroid of the Sun image was estimated to be $p_{row} = 181.197$ (pixels) and $p_{col} = 42.2379$ (pixels), with a confidence of 98.87%. Rover heading with respect to True North was determined to be 154.0154 (degrees). For the sensitivity analysis that follows, the above set of values for the centroid were assumed to the nominal values (99% confidence is close to ideal). To investigate the effect of rover roll uncertainty on the output of the Sun sensor, the norm-bound perturbations of rover roll and pitch were set as follows: $\vartheta_\phi = \pm 2.21$ and $\vartheta_\theta = 0.0$.

Using equation (22) and the above values, the Sun sensor algorithm was run offline. The result is depicted in Figure 16. In the case of rover pitch uncertainty, the perturbation norm-bounds were set as follows: $\vartheta_\phi = 0.0$ and $\vartheta_\theta = \pm 0.13$. The results are shown in Figure 17.
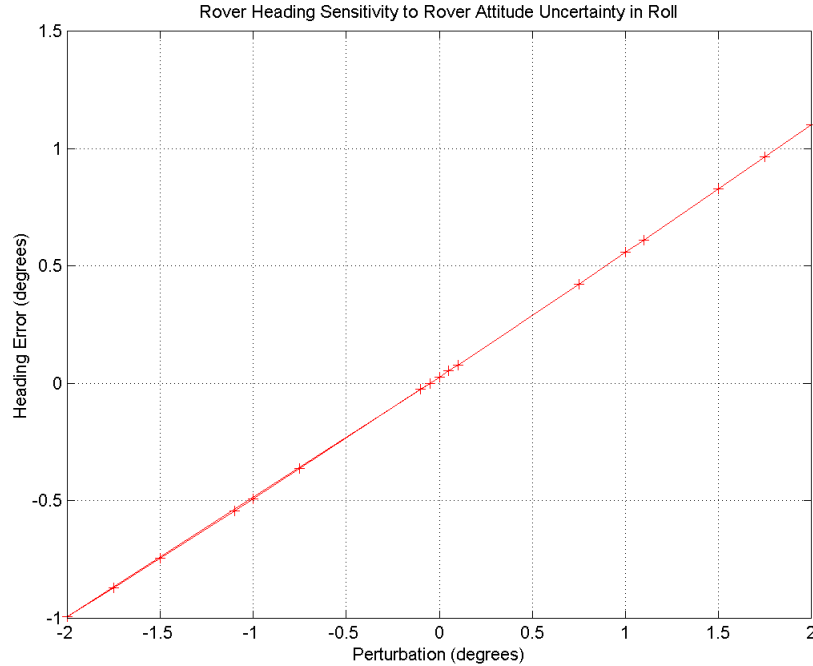


**Figure 16. A Plot of Rover Roll Angle Uncertainty Impact on Sun Sensor Rover Heading Detection**
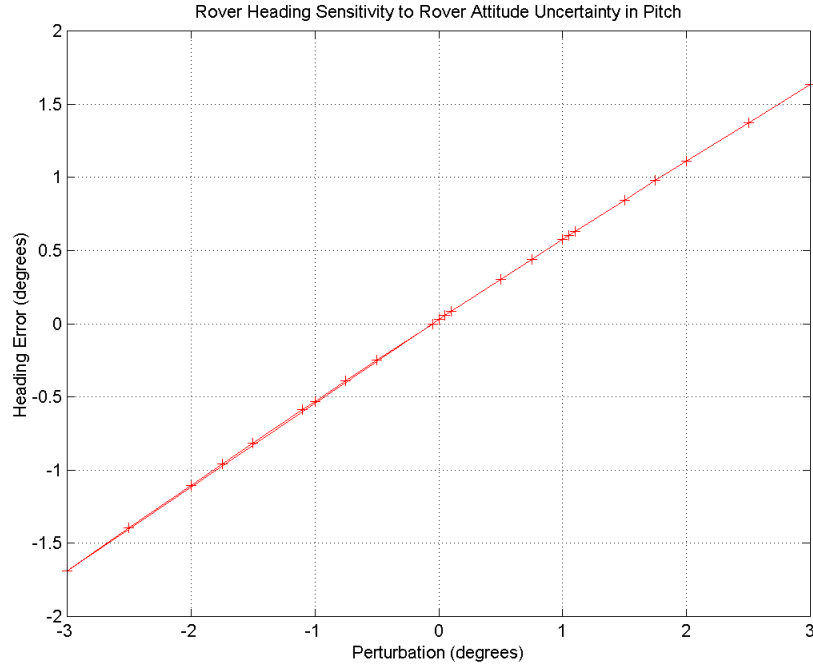
**Figure 17. A Plot of Rover Pitch Angle Uncertainty Impact on Sun Sensor Rover Heading Detection.**

From Figure 16 and Figure 17 we observe that rover attitude uncertainty (in both roll and pitch) $< \pm 2^o$ have no significant effect on the Sun sensor output. However, uncertainties greater $\geq \pm 2^o$ can result in heading errors $\geq \pm 1^o$. In addition, we observe that the attitude uncertainty and its effect on heading error is a linear relation with a gradient of $0.5^o$ rover heading error per degree error in rover attitude. This suggest that if the rover attitude sensor is fairly robust, with a resolution less than a degree, the rover attitude will have no significant effect on the Sun sensor output. In addition to the above offline simulation, we setup an experiment to verify the above findings. The results are presented below.

The result of an experiment conducted with varying rover roll, but fixed rover pitch and heading angles, is presented in Table 1. The experiment covered half the operating envelope of the rover in roll (i.e., 0 to 32 degrees). The experiment results validated the simulation results. However, at 16 and 32 degrees roll there are significant heading errors ($\geq \pm 1^o$). This can be partially attributed to the low confidence Sun images (see Figure 20 and Figure 21). In addition, 2-D centroids are located in between regions 0.1 to 0.20 error/pixel (see Figure 14), compounding any errors. A complete set of Sun images for each roll angle is shown in Figure 18 to Figure 21.

In the same experimental setup, we varied the rover's pitch, with the rover roll and heading fixed. The results of this experiment are presented in Table 2; Sun images for each pitch angle are shown in Figure 22 to Figure 25. The heading errors as expected are less than a degree in line with the simulation results. However, a significant heading error ($\geq \pm 1^o$) is observed at pitch angle of 29 degrees. The non-circularity of the Sun disk (see Figure 25) introduces significant uncertainty in the estimate of the 2-D Sun centroid leading to significant heading error.

The experiments show that a gyroscopic bias of 0.01 degree/ sec would be more than suitable for the Sun sensor because the operation times for planetary rovers are typically of the order of a few hours. The result obtained from these experiments demonstrates that the Sun sensor is robust to rover attitude changes. This attribute will be very useful in rover exploration of valleys and impact craters of the Southern Hemisphere of Mars, where recent sitings suggest that liquid water has seeped out of surface gullies and alluvial fans. In such an environment, incremental odometry heading estimation of a rover is not suitable because the rover wheels would slip often due to the ruggedness of the terrain, leading to huge heading errors.

**Table 1. Experimental Results of Sun Sensor Rover Heading Readings for Varying Rover Roll Angle with Fixed Pitch Angle (-1.2722 deg.) and Rover Heading**

| Rover Roll (degrees) | Time | 2-D Centroid Row (pixels) | 2-D Centroid Column(pixels) | Confidence (%) | Rover Heading (degrees) | Heading Error (degrees) |
|---|---|---|---|---|---|---|
| -0.70188 | 9:59 am | 223.1341 | 27.73171 | 99.0 | 64.47 | 0.23 |
| 7.719 | 10:02 am | 228.8544 | 71.55131 | 97.1 | 65.13 | -0.43 |
| 15.7546 | 10:04 am | 233.3887 | 113.0578 | 97.6 | 65.71 | -1.01 |
| 31.94616 | 10:12 am | 254.0006 | 202.6265 | 89.60 | 62.86 | -1.84 |

**Table 2. Experimental Results of Sun Sensor Rover Heading Readings for Varying Rover Pitch Angle with Fixed Roll Angle (-0.717 Deg.) and Rover Heading**

| Rover Pitch (degrees) | Time | 2-D Centroid Row (pixels) | 2-D Centroid Column(pixels) | Confidence (%) | Rover Heading (degrees) | Heading Error (degrees) |
|---|---|---|---|---|---|---|
| -0.23658 | 10:19 am | 260.9356 | 36.10508 | 99.6 | 62.64 | -0.64 |
| 5.899646 | 10:21 am | 244.1236 | 36.82397 | 99.3 | 62.01 | -0.01 |
| 14.98702 | 10:23 am | 218.1802 | 37.82332 | 98.4 | 61.11 | 0.89 |
| 28.9010 | 10:25 am | 175.1954 | 35.30651 | 98.1 | 60.07 | 1.93 |

**Figure 18. Sun Image at 9:59 am Rover Roll –0.7019 degrees**



**Figure 19. Sun Image at 10:02 am Rover Roll 7.719 degrees**



**Figure 20. Sun Image at 10:04 am Rover Roll 15.7546 degrees**



**Figure 21. Sun Image at 10:12 am Rover Roll 31.946156 degrees**

**Figure 22. Sun Image at 10:19 am Rover Pitch Angle –0.236577 degrees**



**Figure 23. Sun Image at 10:21 am Rover Pitch Angle 5.899646 degrees**



**Figure 24. Sun Image at 10:23 am Rover Pitch Angle 14.987015 degrees**



**Figure 25. Sun Image at 10:25 am Rover Pitch Angle 28.9010 degrees**

### 4.1.3    Impact of the Sun's Elevation on Sun Sensor Output

The Earth travels around the Sun in a circular orbit, with a different tilt angle from the Sun at different times of the year.  This causes seasonal changes on Earth.  For example, the summer Sun is at a higher elevation in the sky than the winter Sun.  In addition, in the early morning or late afternoon (Sunrise or Sunset) the Sun is low in the sky in both the summer and winter.  Typically, the Sun is at an angle that is most nearly vertical near solar noon.

In this section, we will investigate the sensitivity of the Sun sensor output with respect to the Sun's elevation over a 4-hour period (a typical operational period for a planetary rover). The Sun sensor FOV is rather restrictive; hence, the Sun is within the sensor FOV from about 10:00 am to 2:00 pm in the winter. This is only achieved after judicious positioning of the rover. On 31 October 2000 at 10:12 am, the rover was position with attitude, roll = –0.906476 degrees and pitch = –15.446365 degrees such that the Sun was within the view of the Sun sensor. At intervals of 5 minutes, a Sun sensor reading of the rover heading was collected until 1: 57 pm (approximately a 4-hour period). The day was cloudless, effectively eliminating or reducing the influence of atmospheric uncertainties as major factor in the Sun sensor output. The average confidence measure for the Sun images was 97%, confirming a cloudless day. Figure 26 depicts a plot of the Sun's azimuth against elevation for the duration of the experiment. The Sun's elevation and azimuth were obtained from ephemeris data and equation of time. Figure 27 depicts the trace of the 2-D location (centroid) of the Sun in images captured for the duration of the experiment. In contrast to Figure 26, Figure 27 is almost a straight line; the reason for this is that the Sun is at infinity with respect to the Sun sensor. Consequently, the radius of curvature is infinity; hence, the straight line. Also, the 2-D Sun centroid is moving across the image plane from left to right (see Figure 27).

Figure 28 shows the rover heading error against time, which can be interpreted as a plot of rover heading error against Sun elevation. In Figure 28, the heading error follows a quadratic profile with respect to the Sun's elevation. There are two main reasons for this trend. The first reason is that the Sun is moving across the image plane from a region of least error/pixel through the region with the worst error/pixel to a region of least error/pixel (see Figure 14) as discussed in section 4.1.1.1. The second reason is that as the Sun elevation rises the Sun captured in the image is relative large and non-circular (compared to low elevation Sun images). Similarly, at extremely low elevations, the Sun disk is very small and non-circular. The non-circularity and enlarge/very small image of the Sun introduces significant uncertainty in the 2-D Sun centroid estimate, leading to relatively large errors at Sunrise, solar noon, and Sunset. In Figure 28, the Sunrise period corresponds to 10:00 am to 10:30 am; the solar noon period corresponds to 11.45 am to 12.30 pm. Another source of error is the parametric uncertainty in the camera model with respect to the radial distortion of the wide FOV lens. The maximum heading error that occurs about noon is less than a degree. It is safe to conclude that the elevation of the Sun has no significantly impact on the output of the Sun sensor. The results obtained from the experiments would be used to formulate a new bias term in equation (18) to account for elevation of the Sun and the location of the 2-D Sun centroid in the image plane to further reduce the heading error.
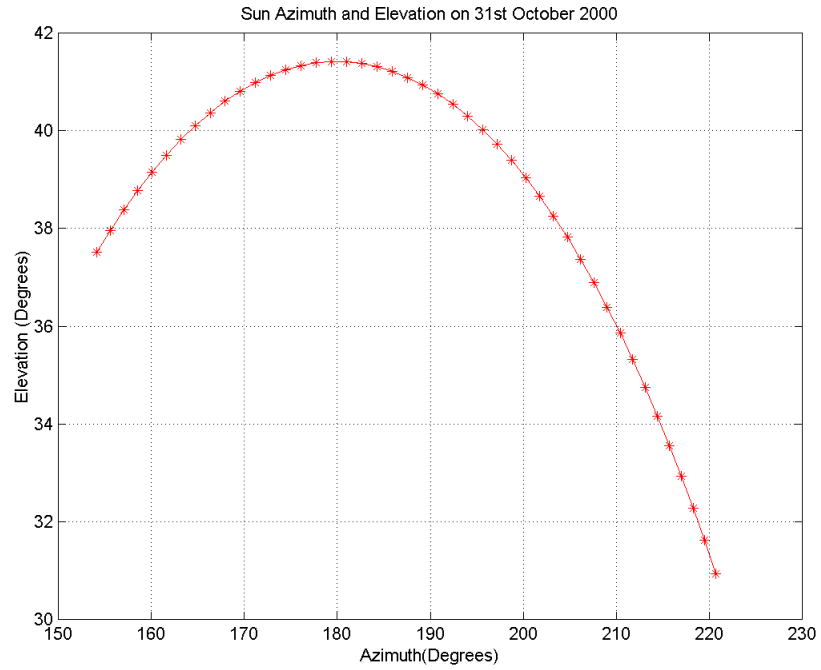
**Figure 26. From a Fixed Location on Earth (JPL), the Sun's Position from 10 am to 2pm on the 31st October 2000 Using Ephemeris Data and Equation of Time**
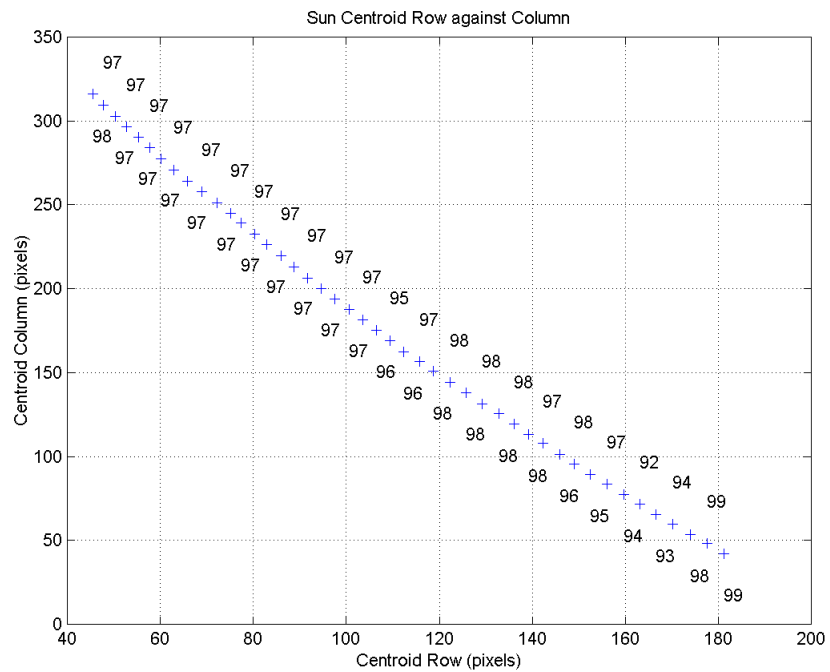


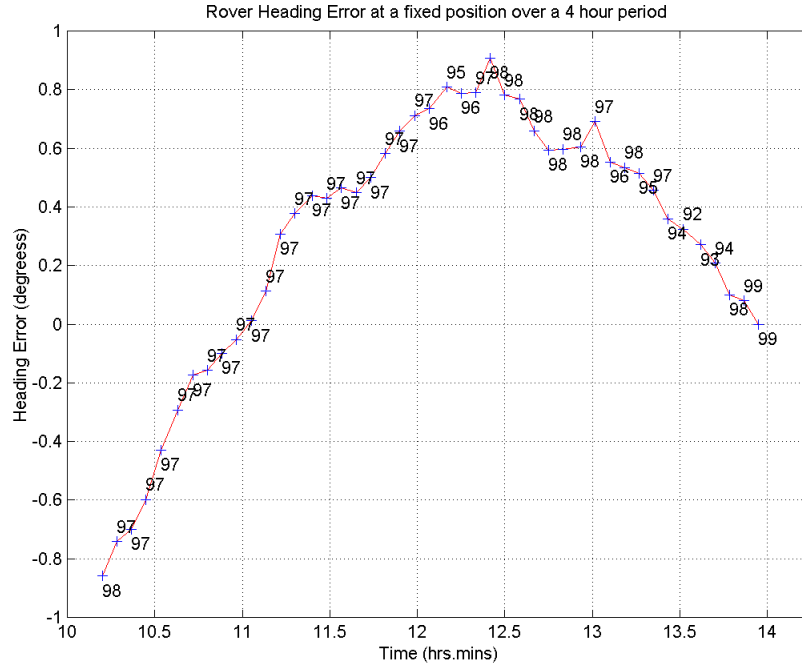**Figure 27. 2-D Location of Sun in Images Taken on the 31st October 2000 from 10 am to 2pm**

**Figure 28. A Plot of Rover Heading Error and Corresponding Confidence over a Four-hour Period at a Fixed Location**

Figure 29 and Figure 30 depict the results of the above experiment conducted a day earlier (October 30, 2000) on a very cloudy day. These results are presented here to demonstrate the robustness of the Sun sensor to certain atmospheric conditions (e.g., clouds) and some limitations of the current Sun algorithm. Figure 29 depicts the trace of the 2-D location (centroid) of the Sun for the duration of the experiment. The average Sun image confidence for the experiment was 82%. Comparing Figure 29 to Figure 27 we observe significant point scatter (the effect of cloud cover). Nevertheless, the point scatter of 2-D Sun location in Figure 29 can be approximated with a straight line. This demonstrates the robustness of the 2-D Sun image centroiding to some atmospheric conditions. Figure 30 further demonstrates the robustness of the Sun sensor algorithm; under varying cloud cover, the heading errors are still within 1 degree (although there is a great deal more fluctuation in the heading error compared to Figure 28, as would be expected). Figure 31 and Figure 32 depict the best Sun images for the day with confidence of about 99%. On the other hand, Figure 33 to Figure 38 depict the five worst Sun images for the day. In Figure 35, it is virtually impossible for the human eye to see the Sun; however, the algorithm was able to detect the Sun location, resulting in the worse heading error, 0.9 degrees, a remarkable fit. In addition, the experiment helped determine the cutoff confidence for a good Sun image, which is $\geq 80\%$.
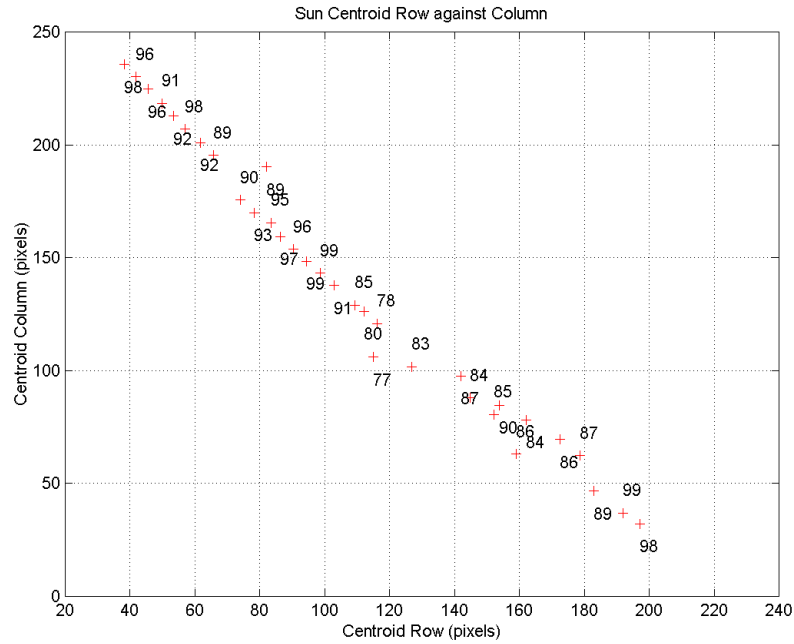
**Figure 29. 2-D Location and Confidence of Sun in Images Taken on the 30<sup>th</sup> October 2000 from 10:30am to 1:40pm**
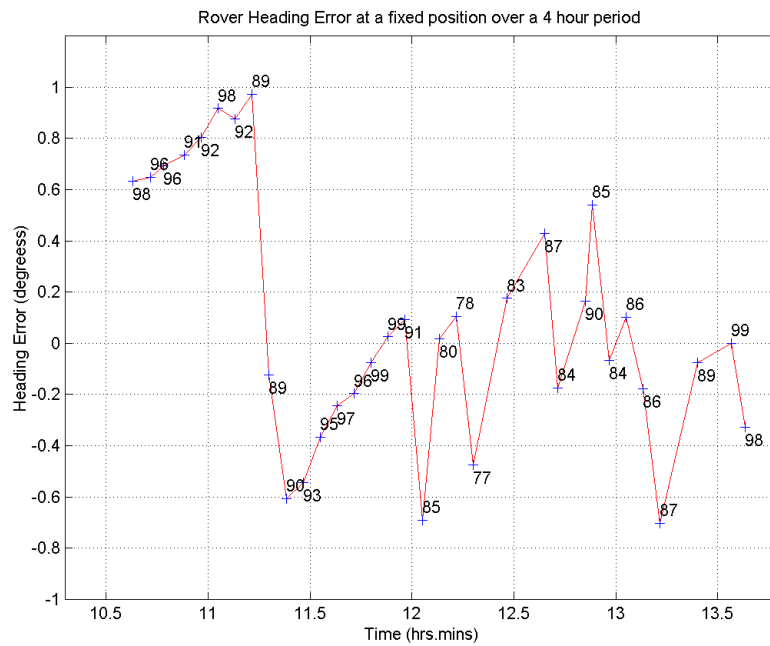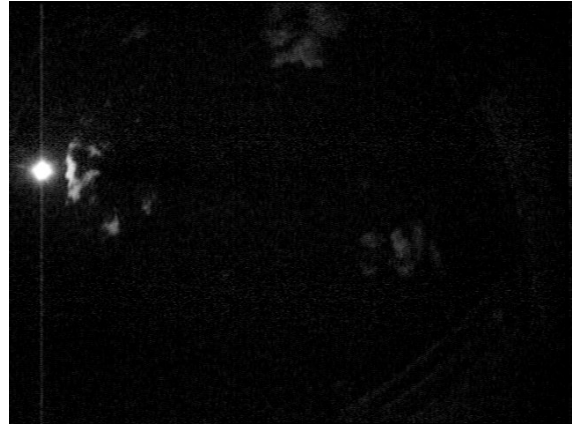


**Figure 30. A Plot of Rover Heading Error and Confidence over a Three-hour Period at a Fixed Location, 30<sup>th</sup> October 2000**

**Figure 31. Sun Image at 11:43am 30ᵗʰ October 2000, confidence 98.55%**
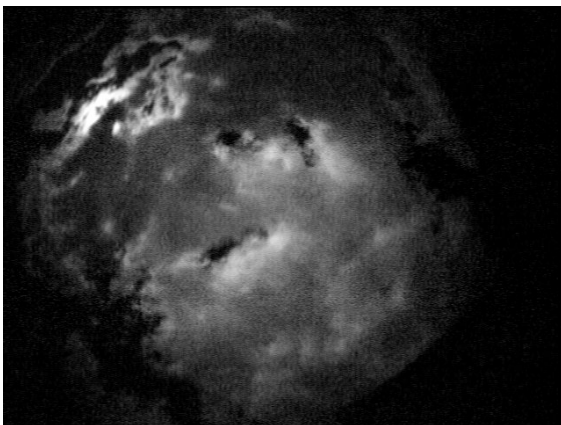


**Figure 32. Sun Image at 1:34pm 30ᵗʰ October 2000, Confidence 99.29%**



**Figure 33. Sun Image at 12:08pm 30ᵗʰ October 2000, Confidence 80.38%**
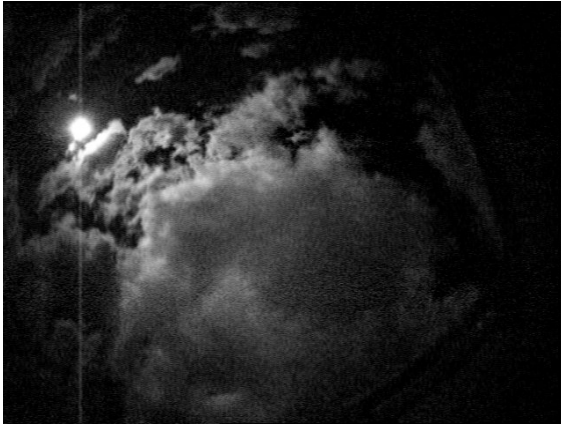


**Figure 34. Sun Image at 12:13pm 30ᵗʰ October 2000, Confidence 77.61%**
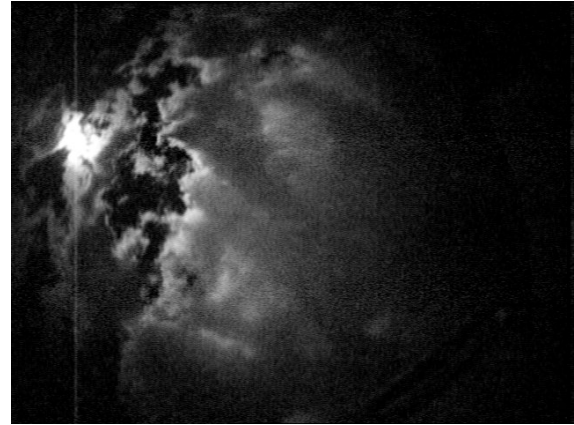


**Figure 35. Sun Image at 12:18pm 30ᵗʰ October 2000, Confidence 76.95%**



**Figure 36. Sun Image at 12:28pm 30ᵗʰ October 2000, Confidence 83.24%**

**Figure 37. Sun Image at 12:43pm 30<sup>th</sup> October 2000, Confidence 84.23%**



**Figure 38. Sun Image at 12:58am 30<sup>th</sup> October 2000, Confidence 84.11%**

## 5  Conclusions

In this paper, we have presented extensive analysis, simulation, and experimental results of a new planetary rover Sun sensor for rover absolute heading detection.  The new sensor can handle the effect of atmospheric conditions (cloud cover), changes in the Sun's position, and uncertainty in rover attitude measurements.  The research reported here has led to a Sun sensor being included in the sensor suite for the NASA 2003 Mars rovers.  One of the key uses for the Sun sensor on the 2003 mission will be to help point the high gain antenna on the rover to Earth and thereby establish communication at the end of a Sol.

A major disadvantage of the current design is the limited field of view of the lens.  Research is currently on the way to develop a $150 \times 150$ FOV Sun sensor.  Another major challenge is the collection of dust on the Sun sensor; this would be a major challenge for a 90-Sol mission, as planned for 2003.  In addition, we are investigating the possible use of the Sun sensor to estimate the rover position during a very long traverse (e.g., $\geq 10 Km$) by employing concepts of solar point or geographic position (GP) of a body on a planet and circles of equal latitude.

## 6  References

1.     Aleksandr Brandt, and, John  F.  Gardner (1998). Constrained Navigation Algorithms for Strapdown Inertial Navigation Systems with Reduced Set of Sensors. American Control Conference, Philadelphia, Pennsylvania.

2.     Baumgartner, E. T. (2000). In-Situ Exploration of Mars Using Rover Systems. AIAA Space 2000 Conference, Long Beach, CA, AIAA.

3.     D. H. Titterton, and, J. L. Weston (1997). Strapdown inertial navigation technology. London, Peter Pergrinus Ltd.

4.  Doraiswami, R., and R. Stephen Price (1998). "A Robust Position Estimation Scheme Using Sun Sensor." <u>IEEE Transaction on Instrumentation and Measurement</u> **47**(2): 595-603.

5.  E. T. Baumgartner, Hrand Aghazarian, A. Trebi-Ollennu, T. L. Huntsberger, and, M. S. Garrett (2000). <u>State Estimation and Vehicle Localization for the FIDO Rover</u>. Sensor Fusion and Decentralized Control in Autonomous Robotic Systems III, SPIE, Boston, MA, SPIE.

6.  Gennery, D. B. (0000). Least-Squares Camera Clibration Including Lens Distortion and Automatic Editing of Calibration Points. <u>To appear in "Calibration and Orientation of Cameras in Computer Vision"</u>. A. G. a. T. Huang, Springer-Verlag.

7.  Levine, M. D. (1985). <u>Vision in Man and Machine</u>. New York, McGraw-Hill.

8.  Moshier, S. L. (1987). Self-contained ephemeris calculator, Astronomy and numerical software source codes website, http://people.ne.mediaone.net/moshier/index.html. **1999**.

9.  Nebot, E., and, Durrant-Whyte, H. (1997). <u>Initial calibration and alignment of an inertial navigation</u>. Fourth Annual Conference on Mechatronics and Machine Vision in Practice.

10. Paul G. Backes, and, Jeffrey S. Norris (2000). Mars Rover Mission Distributed Operations. <u>TMOD Technology and Science Program News</u>.

11. R. E. Arvidson, S. Squyres., E. T. Baumgartner, L. Dorsky, and, P. Schenker (2000). "Rover Trials for Mars Sample Return Mission Prove Successful." <u>EOS Transactions, American Geophysical Union</u> **81**(7): 65-72.

12. R.M. Haralick, S. R. Sternberg., and, X. Zhuang (1987). "Image analysis using mathematical morphology." <u>IEEE Trans. PAMI</u> **9**(4): 532-550.

13. Randel Lindemann, Lisa Reid, and, Chris Voorhees (1999). <u>Mobility Sub-System for the Exploration Technology Rover</u>. 33rd Aerospace Mechanisms Symposium.

14. Volpe, R. (1999). <u>Mars Rover Navigation Results Using Sun Sensor Heading Determination</u>. 1999 IEEE/RSJ International Conference on Intelligent Robot and Systems.

15. Wertz, J. R. (1995). <u>Spacecraft Attitude Determination and Control</u>, Kluwer Academic Publishers.

16. Y. Xiong, and, K. Turkowski (1997). <u>Creating image-based VR using self-calibrating fisheye lens</u>. IEEE conference on Computer Vision and Pattern Recongnition.

# REPORT DOCUMENTATION PAGE

| 1. AGENCY USE ONLY (*Leave blank*) | 2. REPORT DATE<br>January 26, 2001 | 3. REPORT TYPE AND DATES COVERED<br>Final | |
|---|---|---|---|

**4. TITLE AND SUBTITLE**

Design and Analysis of a Sun Sensor for Planetary Rover Absolute Heading Detection

**5. FUNDING NUMBERS**

TA 100097 RMSA.R.A

**6. AUTHOR(S)**

Ashitey Trebi-Ollennu, Terry Huntsberger, Yang Cheng, E. T. Baumgartner, and Brett Kennedy

**7. PERFORMING ORGANIZATION NAME(S) AND ADDRESS(ES)**

Jet Propulsion Laboratory,
California Institute of Technology
4800 Oak Grove Drive, Pasadena, California 91109

**8. PERFORMING ORGANIZATION REPORT NUMBER**

NASA-CR-2001-210800

**9. SPONSORING/MONITORING AGENCY NAME(S) AND ADDRESS(ES)**

National Aeronautics and Space Administration
Washington, DC 20546-0001

**10. SPONSORING/MONITORING AGENCY REPORT NUMBER**

NASA-CR-2001-210800

**11. SUPPLEMENTARY NOTES**

**12a. DISTRIBUTION/AVAILABILITY STATEMENT**

Subject Category: 19      Distribution: Standard
Availability: NASA CASI (301) 621-0390

**12b. DISTRIBUTION CODE**

**13. ABSTRACT** *(Maximum 200 words)*

This paper describes a new Sun sensor for absolute heading detection developed for the Field Integrated, Design and Operations (FIDO) rover. The FIDO rover is an advanced technology rover that is a terrestrial prototype of the rovers NASA/Jet Propulsion Laboratory (JPL) plans to send to Mars in 2003. The need for a Sun-sensor on planetary rovers lies in the fact that current means of estimating the heading of planetary rovers involves integration of noisy rotational-speed measurements. This noise causes error to accumulate and grow rapidly. Moreover, the heading error affects the estimate of the x, y position of the rover. More importantly, incremental odometry heading estimation is only reliable over relatively short distances. There is an urgent need to develop a new heading-detection sensor for long traverses (for example, 100 m per Sol [Martian Day]), as outlined for the 2003 Mars mission. Results of a recent FIDO field trial at Black Rock Summit in Central Nevada and several Operations Readiness Test (ORTs) at the JPL MarsYard using the Sun-sensor have demonstrated three- to four-fold improvement in the heading estimation of the rover compared to incremental odometry. These test results helped shape the mission

**14. SUBJECT TERMS**

Planetary Rover, Sun Sensor, Heading Estimation

**15. NUMBER OF PAGES**

36

**16. PRICE CODE**

| 17. SECURITY CLASSIFICATION OF REPORT<br>Unclassified | 18. SECURITY CLASSIFICATION OF THIS PAGE<br>Unclassified | 19. SECURITY CLASSIFICATION OF ABSTRACT<br>Unclassified | 20. LIMITATION OF ABSTRACT<br>UL |
|---|---|---|---|